Non-isothermal kinetic analysis of the oxidation of Al–50Mg powder mixture

Mohammad Soltani[1] · **Amir Seifoddini**[1] · **Saeed Hasani**[1] ·
Parisa Rezaei-Shahreza[1]

Abstract

In this research, non-isothermal kinetic analysis of the oxidation process of Al–50Mg (wt%) powder mixture was performed by employing differential scanning calorimetry and thermogravimetry analysis techniques. The research findings revealed that oxidation of this powder mixture was completed at lower temperatures compared to that of pure aluminum powder; and furthermore, it enjoyed a higher thermal efficiency than that of pure magnesium powder. Oxidation of this mixture powder led to the formation of magnesium oxide (MgO) and spinel phase ($MgAl_2O_4$) during the first and second oxidation steps, respectively. Moreover, to calculate the activation energy (E) over a wide range of degree of conversion (α), two isoconversional methods, including Starink and Friedman methods were used. Activation energies decreased as the reaction progressed at both stages, indicating that these stages were multi-step reactions. Furthermore, the invariant kinetic parameter method and fitting model were used to determine the empirical kinetic triplets (i.e. E, pre-exponential factor (A) and reaction model ($g(\alpha)$)). The obtained results showed that the first stage was controlled by the second order Avrami-Erofeev mechanism (A_2), two-dimensional phase boundary reaction (R_2), and two-dimensional diffusion (D_2) models at heating rates of 5, 10, and 30 °C/min. The second stage was controlled by the third order Avrami-Erofeev mechanism (A_3) and A_2 at heating rates of 5 and 10 °C/min, while for a heating rate of 30 °C/min, the mechanism of reaction changes from A_3 to A_2.

Keywords Oxidation process · Kinetic analysis · Activation energy · Isoconversional methods · Fitting models

✉ Saeed Hasani
hasani@yazd.ac.ir

1 Department of Mining and Metallurgical Engineering, Yazd University, Yazd 89195-741, Iran

Introduction

Metal-based energetic materials are used in many applications such as termites [1, 2], energy storage, and pyrotechnics and explosives [3]. Light metal powders such as aluminum, magnesium and titanium can be added as high energy components to solid fuel or used as a metal suspension in hydrocarbon fuel [4]. Thermodynamic calculations indicate that the enthalpy of oxidation process of these metal-based energetic materials is higher than that of the hydrocarbon fuels [4, 5]. Among these metals, Aluminum powder is known as the most common metal additive due to its unique properties such as high enthalpy of its oxidation and relatively low cost [6–8].

The effect of oxidizing atmosphere [9–11], particle size [12], and heating rate [8] on the oxidation of aluminum powders has been investigated by researchers. Zhu et al. [10] studied the oxidation of aluminum powder in CO_2 and CO_2/O_2 mixed oxidizers. They showed that the main characteristic of oxidation of aluminum powder in CO_2 environment compared with that of O_2 was the broadening of the γ-Al_2O_3 to α-Al_2O_3 phase transformation, so that it leads to fuller oxidation in CO_2 environment. Also, the kinetics of the oxidation process of aluminum powder in the temperature range of 1000–1150 °C was performed in previous publications [13–15]. It is shown that the oxidation of these particles as a multi-step reaction is controlled by the Avrami–Erofeev model and the values of activation energies were calculated equal to 150–160 kJ/mol [13]. However, it has been accepted that oxidation of the aluminum powder particles is not completed even up to 1400 °C due to the presence of a protective oxide layer [14–17].

Magnesium powder particles are known as a high energy material, which can be oxidized without the presence of a protective oxide layer [18, 19]. Chunmiao et al. [11] showed that the non-isothermal magnesium powder oxidation under air atmosphere occurs in three stages. Although combustion enthalpy of the Mg powder particles is lower than that of the aluminum powder [20, 21], magnesium powder has a higher burning rate [22] with lower ignition temperature [21], which has attracted the attention of many researchers [5, 11, 23, 24]. Hence, they have focused on Al-based alloy powders such as Al–Mg, Al–Ti, and Al–Li to reduce the combustion delay [25, 26], and to increase burn rate [21, 27], and thermal efficiency [28, 29]. On the other hand, mixing metal powders can also be as another effective method [30–32], while the oxidation mechanism of these materials has not attracted much attention of researchers.

Therefore, in the present study, the oxidation mechanism of Al–Mg powder mixture is investigated. For this purpose, the kinetic parameters including activation energy (E), pre-exponential factor (A), and reaction model ($g(\alpha)$) were calculated by using the isoconversional methods (Starink [33, 34] and FR [35] methods) in combination with invariant kinetic parameter (IKP) [36] and fitting [37, 38] methods.

Table 1 The specifications of the raw materials

Material	Size (μm)	Purity (%)	Company
Al	< 100	99.00	MERCK
Mg	< 63	99.66	Yazd Powder Metallurgy, Iran

Table 2 Chemical composition of the Mg powder used in this study (measured by ICP-OS)

Elements	Mg	Ca	K	Al	Si	Fe
Composition (wt%)	99.656	0.120	0.094	0.070	0.040	0.020

Materials and methods

Materials and testing process

The powder mixture of Al50–Mg50 (in weight percentage) was prepared using the materials listed in Table 1.

To characterize the chemical composition of the used commercial magnesium powder, the coupled plasma optical spectroscopy (ICP-OS) technique was employed and the results are listed in Table 2.

To prepare the powder mixture, the reagents are mixed in a can by mini gearbox engine (Ming Jong Electric Co.) for 6 h with a speed of 4 rpm. Thermogravimetry (TGA) and differential scanning calorimetry (DSC) techniques were used by a Simultaneous Thermal Analysis (STA) device (NETZSCH STA 409 PC/PG) at various heating rates of 5, 10, 20, and 30 °C/min up to 1200 °C. The DSC/TGA analysis was carried out on approximately 25 mg quantities of powder mixture samples with sensitivity of ± 10 μW under air flow supplied at the rate of 30 mL/min. Based on the DSC/TGA curves, the characteristics temperatures of the oxidation process were determined.

For a detailed understanding of the oxidation process, the mixture powder samples were heated at a heating rate of 20 °C/min under air atmosphere up to the characteristics temperatures determined by DSC/TGA curves (500, 750, and 1000 °C). Then, these samples were subjected to phase analysis by using X-ray diffraction (XRD, Philips PW1730) with a Cu target (Cu K_α, $\lambda = 0.15418$ nm) radiation generated at a voltage of 40 kV and current of 30 mA. The samples were scanned in an interval of $10° < \theta < 90°$ and at a scanning rate 1°/min with a step size of 0.05° in a continuous mode. XRD analysis of the investigated samples was performed using X'pert High Score software (3.0.5) in comparison with the reference powder diffraction data given by the Joint Committee on Powder Diffraction Standards (JCPDS). Also, microstructural observations were performed by using a scanning electron microscope (SEM, FEI ESEM QUANTA 200). The samples were gold coated for 240 s in a sputter coater in an Ar atmosphere before loading in SEM. The electrons at 20 kV sources were used to develop relevant information about the samples. The semiquantitative chemical analysis was carried out by energy-dispersive x-ray

spectrometry (EDX, EDAX EDS Silicon Drift 2017), coupled to the scanning electron microscope.

Kinetic analysis

The values of the degree of conversion (α) at any given temperature and heating rate were calculated by using the peaks of DSC curves as follows [39]:

$$\alpha = \frac{A_x}{A_\infty} \tag{1}$$

Here A_x is the peak area from the start temperature of reaction to a specified temperature (T) and A_∞ is the total peak area.

To perform a comprehensive kinetic analysis, the isoconversional methods in combination with the fitting models are used [38–44]. Therefore, the kinetics of oxidation of powder mixture has been investigated by these methods.

Isoconversional methods

The isoconversional methods are used to obtain activation energy (E) and its dependence on α regardless of the reaction model, [38, 45, 46]. Among these methods, Starink and FR can be used to calculate more accurate values of E [47].

The integral Starink [33, 34] and differential FR [35] isoconversional methods are based on Eqs. 2 and 3, respectively:

$$\ln \frac{\beta}{T^{1.92}} = \text{const.} - 1.0008 \frac{E}{RT} \tag{2}$$

$$\ln \left[\beta \left(\frac{d\alpha}{dT} \right) \right] = \ln \left[Af(\alpha) \right] - \frac{E}{RT} \tag{3}$$

Here α is the degree of conversion, β is the linear heating rate (°C/min), T is the absolute temperature (K), R is the general gas constant (J/mol K), and E is the activation energy (kJ/mol).

For $\alpha = \text{const.}$, the E values can be evaluated from the slope of the plots of $\ln(\beta/T^{1.92})$ vs. $1/T$ and $\ln[\beta \, (d\alpha/dT)]$ vs. $1/T$ without knowing the reaction model.

Invariant kinetic parameter (IKP) method

In this method, invariant kinetic parameter including E_{inv} and A_{inv} values are obtained with the intersection of $\ln A$ versus E curves in an appropriate kinetic model [36]. For this purpose, the values of $E_{g(\alpha)}$ and $\ln A_{g(\alpha)}$ are achieved for all heating rates and algebraic expressions ($g(\alpha)$) (which have been presented in the previous publications [38, 40, 48]) by using the Coats-Redfern (CR) [49] method (Eq. 4).

$$\ln \frac{g(\alpha)}{T^2} \cong \ln \frac{AR}{\beta E} - \frac{E}{RT} \tag{4}$$

According to IKP method, there is a linear relationship between the values of E and $\ln A$ at each heating rate (Eq. 5). So, the lines drawn at various heating rates intersect at a given point, if there is a constant mechanism. This intersection represents values of E_{inv} and $\ln A_{inv}$ for the correct reaction model [36].

$$\ln A_i = a + bE_i \tag{5}$$

In Eq. 5, subscript ''i'' represents the heating rate; a and b are the compensation effect parameters.

Fitting models

As mentioned, the isoconversional methods determine the activation energy without determining the reaction model and the pre-exponential factor. Therefore, the fitting models are used not only to validate the results obtained by isoconversional and IKP methods but also to determine two other kinetic parameters [37, 38]. According to the fitting model, the reaction model is specified by plotting experimental and theoretical data of $g(\alpha)$ and obtain the best matching between them. The theoretical curves of $g(\alpha)$ as a function of α can be plotted by using the algebraic expressions for $g(\alpha)$, which have been indicated in the previous literature [38–40, 48]. The experimental curves of $g(\alpha)$ as a function of α can be plotted by using the following Eq. 6.

$$g(\alpha) = \frac{A}{\beta} \int_0^T \exp\left(-\frac{E}{RT}\right) dT \tag{6}$$

Here the temperature integral in Eq. 6 $\int_0^T \exp(-\frac{E}{RT}) dT$ is determined by Eq. 7 [50];

$$\int_0^T \exp\left(-\frac{E}{RT}\right) dT = \frac{RT^2}{E + 2RT} \exp\left(-\frac{E}{RT}\right) \tag{7}$$

Results and discussion

Thermal analysis

Fig. 1 displays the DSC and TGA curves of the Al–Mg powder mixture. As shown, there are two exothermic peaks at different heating rates, corresponding to the extreme weight gain in the TG curves. Thus, the oxidation process of the powder mixture is carried out in two steps. On the other hand, it is shown that the oxidation steps shift to higher temperatures with an increase in heating rate, which can be attributed to thermally activated process [51–54]. These results are in a good agreement with other thermally activated processes [55, 56].
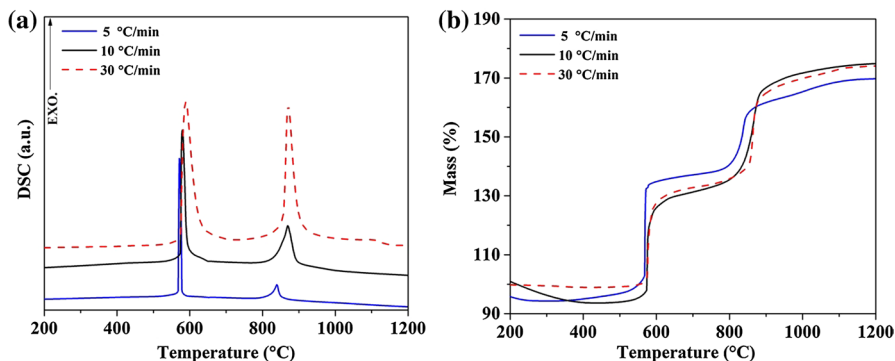
Fig. 1 **a** DSC and **b** TG plots of the oxidation of Al–Mg powder mixture at various heating rates under air atmosphere

Fig. S1 illustrates the DSC curves related to the pure Mg and Al powders and Al–Mg powder mixture at a heating rate of 20 °C/min. By comparing the two DSC curves of magnesium powder particles (Fig. S1) and the powder mixture (Fig. 1a), it is illuminated that the first peak of the DSC curve of the powder mixture is related to the oxidation of magnesium powder particles in the powder mixture.

On the other hand, the DSC curve of Al powder particles (Fig. S1) represents an endothermic peak and an exothermic peak, which are related to the melting of aluminum at 660 °C and the partial oxidation of these particles at 1060 °C [13–15, 57]. Therefore, it is concluded that a small endothermic peak observed in the DSC curve of the Al–Mg powder mixture at a heating rate of 10 °C (Fig. 1a) can be related to the melting of Al (~660 °C). Moreover, previous publications [13, 14] showed that there is a great amount of residual aluminum in the pure Al powder particles heated up to 1200 °C. While, the DSC curve of Al–Mg mixture particles shows that aluminum powder particles in the Al–Mg powder mixture are oxidized at lower temperature (880 °C) compared to that of pure aluminum powder particles (1060 °C).

Phase analysis

The XRD patterns of the raw powder mixture and the samples annealed at a heating rate of 20 °C/min up to the selected temperatures in accordance with the DSC curves are shown in Fig. 2. As seen, only Al and Mg peaks (JCPDS card No. 001-1176 and 03-065-3365) are observed in the XRD patterns of both the raw sample and the sample annealed up to 500 °C, indicating that no oxidation occurs up to 500 °C, which is in agreement with the DSC curve.

With an increase in maximum temperature up to 750 °C, aluminum, magnesium oxide (MgO; JCPDS card No. 01-075-1525) and spinel (MgAl$_2$O$_4$; JCPDS card No. 01-075-1797) phases are identified in the XRD pattern. Therefore, it is confirmed that only the magnesium oxidation is carried out at the first peak of the DSC curves according to the following reaction [11]:
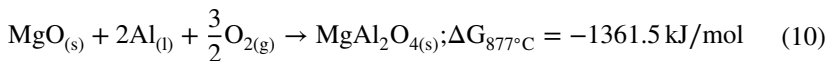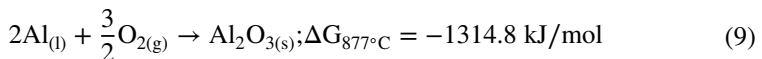
Fig. 2 XRD patterns related to the raw Al–Mg powder mixture and the samples annealed from ambient temperature up to various temperatures at a heating rate of 20 °C/min under air atmosphere

$$Mg_{(s)} + \frac{1}{2}O_{2(g)} \rightarrow MgO_{(s)}; \Delta G_{577\,°C} = -510 kJ/mol \qquad (8)$$
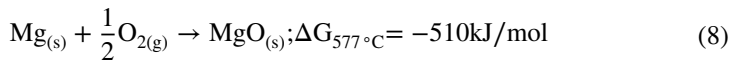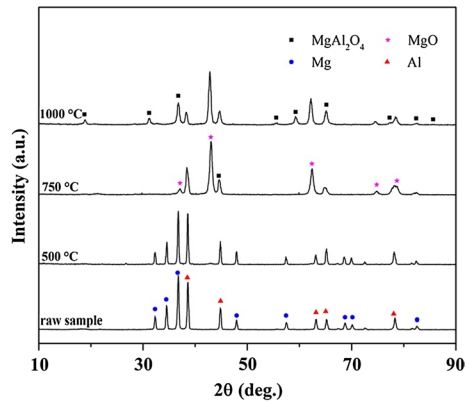
The presence of a protective oxide layer on the surface of aluminum particles delays their oxidation; therefore, this process does not start until the temperature reaches 800 °C. Nevertheless, it is observed that the oxidation of aluminum particles in the powder mixture begins at lower temperatures than in pure aluminum particles, which can be attributed to the reduction of the strength of the protective oxide layer as a result of the oxidation in the first stage.

It is reported that the expansion of the aluminum melt inside the crust can play a significant role to overcome the strength of the crust [15]. Thermal stresses caused by oxidation of the first stage cause the oxidation of aluminum particles in the second stage at lower temperatures. Therefore, this powder mixture can be considered as a solid fuel.

In the second stage of oxidation, the following two reactions is taken place by tearing the oxide shell [23]:

$$2Al_{(l)} + \frac{3}{2}O_{2(g)} \rightarrow Al_2O_{3(s)}; \Delta G_{877\,°C} = -1314.8 \text{ kJ/mol} \qquad (9)$$

$$MgO_{(s)} + 2Al_{(l)} + \frac{3}{2}O_{2(g)} \rightarrow MgAl_2O_{4(s)}; \Delta G_{877\,°C} = -1361.5 \text{ kJ/mol} \qquad (10)$$

As shown in Fig. 2, XRD pattern of the sample annealed up to 1000 °C confirms the existence of spinel phase ($MgAl_2O_4$). Therefore, the second stage of oxidation of the powder mixture can be accompanied by the formation of $MgAl_2O_4$ (reaction (10)). This spinel phase ($MgAl_2O_4$) has a Pilling–Bedworth ratio greater than one (1.30) [23, 58], indicating that this phase can form a continuous oxide film on the surface of the remaining aluminum, which can prevent the remaining aluminum from oxidizing. Therefore, the aluminum peaks appear in XRD pattern of the sample annealed up to 1000 °C. The thermodynamic calculations of

reactions (9) and (10) also show that the reaction (10) is preferable, which is in a good agreement with the obtained results.

Microstructural observation

Fig. S2 represents the SEM micrograph and EDS map of the raw powder mixture. Also, SEM micrograph and EDS map of the sample annealed up to 500 °C are shown in Fig. S3. As seen, no oxidation occurs in the powder mixture by heating up to 500 °C. In our previous publication [20], it was revealed that $Mg(OH)_2$ with a Pilling–Bedworth ratio of 1.76 is formed as a thin continuous oxide layer on the surface of magnesium particles; therefore, this layer can prevent the oxidation of these particles up to ~500 °C. Therefore, no significant oxidation should be expected up to 500 °C, which is in accordance with the phase and microstructural analyses of the sample annealed up to 500 °C.

At temperatures above 500 °C, where $Mg(OH)_2$ is unstable and converts to MgO with a Pilling–Bedworth ratio of 0.81, cannot serve as a barrier layer [20, 59]. Fig. S4 represents the SEM micrograph and EDS map of the sample annealed up to 750 °C. Unlike aluminum particles, magnesium particles are oxidized in this sample.

Fig. S5 shows the SEM micrograph and EDS analysis of the sample heated up to 1000 °C. As seen, the phenomena related to the oxidation of aluminum particles such as bursting of the protective shell of Al particles, oxidation of these particles, and the resulting agglomeration of the particles are well proven in this figure. The yellow arrow indicates the tearing of the alumina shell on the surface of the aluminum particles. Also, the stoichiometry of the formed phase and the theoretical one are compared in Table 3 to better understand the phase formed in this sample. As listed, the presence of the MgO and $MgAl_2O_4$ phases are confirmed in areas 1 and 2, respectively.

Table 3　Elemental composition of the phases formed in the sample heated up to 1000 °C as evaluated from the stoichiometry composition and EDS

Elemental composition evaluated from	Mg (at.%)	Al (at.%)	O (at.%)
Stoichiometry composition			
MgO	50.00	–	50.00
$MgAl_2O_4$	14.29	28.57	57.14
EDS			
Area 1	48.53	9.60	41.87
Area 2	26.53	34.58	38.89

Table 4 Kinetic parameters obtained by isoconversional, IKP, and fitting methods

Peak No	Heating rate (°C/min)	T (°C)		Isoconversional method E (kJ/mol)		Fitting method	
		T_s^a	T_f^b	Starink	Friedman	$\ln A$ (min^{-1})	Model
I	5	568	578	354–901	318–866	85 ± 3	A_2
	10	574	591			81 ± 5	R_2
	30	575	619			83 ± 2	D_2
II	5	821	880	346–482	348–512	46 ± 2	A_3
	10	834	892			48 ± 3	A_2
	30	857	897			51 ± 5	$A_3 \rightarrow A_2$

[a]Start temperature (T_s) of the peaks

[b]Finish temperature (T_f) of the peaks
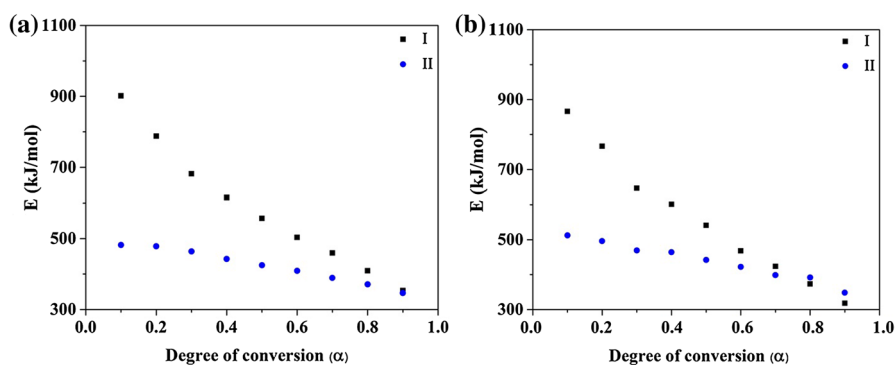
Fig. 3 The dependence of E on α evaluated for two oxidation steps of the oxidation of Al–Mg powder mixture under air atmosphere; calculated by isoconversional **a** Starink and **b** FR methods

Kinetic analysis

Isoconversional methods

Fig. S6 displays the plots of α vs. T for the two steps of oxidation process of the powder mixture at various heating rates. The characteristic temperatures extracted from DSC/TGA curves are listed in Table 4.

The plots of E vs. α are shown in Fig. 3. As seen, the activation energy calculated for the first peak is strongly dependent on α, while for the second peak, this dependence is less expressed (in the range of $0.1 \leq \alpha \leq 0.9$), indicating that there is no unique kinetic mechanism for each of these two oxidation steps. In other words, both stages are multi-step reactions.

Also, the ranges of activation energy determined by both isoconversional methods are listed in Table 4. However, the values of activation energy evaluated by the Starink and Friedman methods are in good agreement with each other.

IKP method

The values of E and ln$A$ for every kinetic model at each heating rate are obtained using the CR method (Eq. 4). Fig. 4 represents the linear relationship between E and ln$A$ for both oxidation stages at various heating rates.

As shown, these lines do not intersect at a given point, indicating that the certain E and ln$A$ cannot be achieved. Hence, the results of isoconversional methods that both stages are multi-step reactions are confirmed by the IKP method.

Fitting models

The fitting method is used to determine the reaction model for both oxidation steps. Fig. 5 represents the theoretical and experimental $g(\alpha)$ vs. α curves for the first and the second steps of oxidation process of the powder mixture at various heating rates.
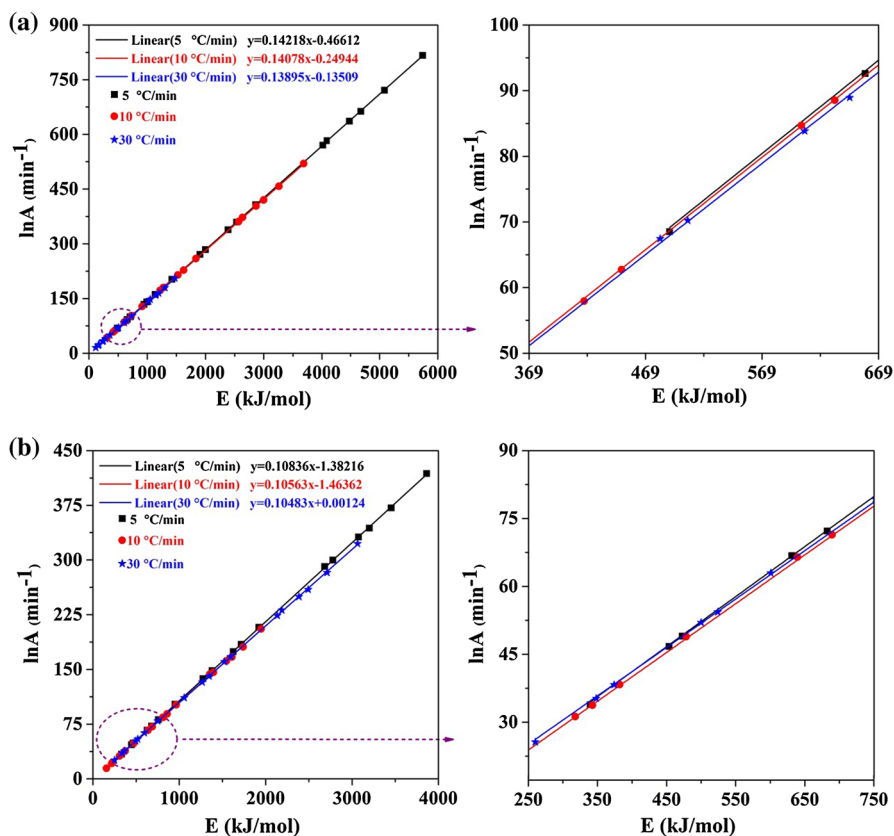

Fig. 4 The compensation relationship and its enlarged region for the **a** first and **b** second oxidation stages of Al–Mg powder mixture under air atmosphere; calculated by IKP method
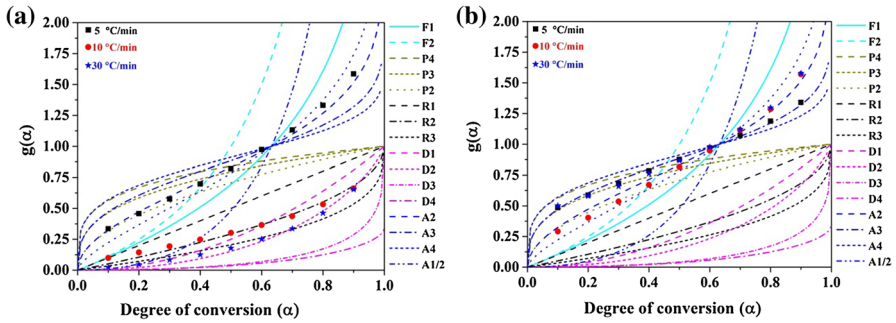
Fig. 5 Plots of the experimental and theoretical $g(\alpha)$ vs. α for the **a** first and **b** second oxidation stages of Al–Mg powder mixture under air atmosphere

The results obtained from these curves are reported in Table 4. As presented, these results are in a good agreement with that obtained by isoconversional and IKP methods. Also, for the first oxidation stage, it is seen that this stage is controlled by A_2, R_2, and D_2 at the heating rates of 5, 10, and 30 °C/min. Moser et al. [5] performed a non-isothermal kinetic analysis on the oxidation of pure magnesium powder and showed that this process was controlled with A_2 model at heating rates less than 5 °C/min. This model demonstrated that the oxidation is controlled by the nuclei growth rate of MgO that is proportional to two-dimensional diffusion [60].

At a heating rate of 10 °C/min, the reaction follows the R_2 model. According to this model, nucleation occurs rapidly on the surface of the crystal and the reaction is controlled by the resulting reaction interface progressing towards the center [60].

At a heating rate of 30 °C/min, the D_2 model (two-dimensional diffusional model) is determined for the reaction. At a high heating rate, the product formation rate (MgO) occurs relatively fast, which can lead to the concentration gradient of oxygen around the magnesium powders. Therefore, the diffusion of oxygen controls the reaction rate. Unlike the first stage of oxidation, in the second stage of oxidation, the reaction follows Avrami-Erofeev models at all three heating rates. This oxidation stage follows the A_3 and A_2 models at heating rates of 5 and 10 °C/min, respectively. However, the reaction model changes from A_3 to A_2 in $\alpha = 0.5$ at a heating rate of 30 °C/min. Hence, the second step of oxidation is controlled by the nucleation and nuclei growth rate of $MgAl_2O_4$, so that the growth rate of nuclei is proportional to the interphase area [61, 62].

Conclusions

In the present research, non-isothermal kinetic analysis of the oxidation process in the Al–Mg powder mixture was investigated. According to DSC-TGA results, this oxidation process of the Al–Mg powder mixture was divided into two stages. Phase analysis revealed that only the magnesium powder particles were oxidized during the first step of the process. During the second oxidation step, the protective oxide layer on the surface of aluminum particles was broken and the spinel phase

($MgAl_2O_4$) was formed due to the contact of aluminum melt with the magnesium oxide (MgO) formed in the first step. Moreover, the obtained results revealed that aluminum powder particles in the powder mixture is oxidized at lower temperatures and more completely compared with pure aluminum powder. Furthermore, activation energy of two oxidation stages of the Al–Mg powder mixture was calculated by isoconversional Starink and Friedman methods. At both stages, the activation energy obtained decreased as the reaction progressed. IKP method also confirmed the results of the isoconversional method. Based on the results obtained by fitting method, the first oxidation stage was controlled by A_2, R_2, and D_2 models at the heating rates of 5, 10 and 30 °C/min. In the second step, the reaction followed the A_3 and A_2 models at heating rates of 5 and 10 °C/min, respectively, and the reaction model changed from A_3 to A_2 at $\alpha = 0.50$ at the heating rate of 30 °C/min.

References

1. Wen D (2010) Nanofuel as a potential secondary energy carrier. Energy Environ Sci 3:591. https://doi.org/10.1039/b906384f
2. Tanvir S, Qiao L (2015) Effect of addition of energetic nanoparticles on droplet-burning rate of liquid fuels. J Propuls Power 31:408–415. https://doi.org/10.2514/1.B35500
3. Velasco F, Guzmán S, Moral C, Bautista A (2013) Oxidation of micro-sized aluminium particles: hollow alumina spheres. Oxid Met 80:403–422. https://doi.org/10.1007/s11085-013-9408-9
4. Goroshin S, Higgins A, Kamel M (2001) Powdered metals as fuel for hypersonic ramjets. 37th Jt Propuls Conf Exhib 1:AIAA-2001–3919. ****https://doi.org/10.2514/6.2001-3919
5. Moser G, Tschamber V, Schönnenbeck C et al (2019) Non-isothermal oxidation and kinetic analysis of pure magnesium powder. J Therm Anal Calorim 136:2145–2155. https://doi.org/10.1007/s10973-018-7845-z
6. Trunov M, Schoenitz M, Dreizin E (2005) Ignition of aluminum powders under different experimental conditions. Propellants Explos Pyrotech 30:36–43. https://doi.org/10.1002/prep.200400083
7. Nie H, Schoenitz M, Dreizin EL (2016) Initial stages of oxidation of aluminum powder in oxygen. J Therm Anal Calorim 125:129–141. https://doi.org/10.1007/s10973-016-5369-y
8. Schoenitz M, Patel B, Agboh O, Dreizin EL (2010) Oxidation of aluminum powders at high heating rates. Thermochim Acta 507–508:115–122. https://doi.org/10.1016/j.tca.2010.05.010
9. Rouillard F, Cabet C, Wolski K, Pijolat M (2009) Oxidation of a chromia-forming nickel base alloy at high temperature in mixed diluted CO/H_2O atmospheres. Corros Sci 51:752–760. https://doi.org/10.1016/j.corsci.2009.01.019
10. Zhu X, Schoenitz M, Dreizin EL (2009) Aluminum powder oxidation in CO_2 and mixed CO_2/O_2 environments. J Phys Chem C 113:6768–6773. https://doi.org/10.1021/jp809816u
11. Chunmiao Y, Lifu Y, Chang L et al (2013) Thermal analysis of magnesium reactions with nitrogen/oxygen gas mixtures. J Hazard Mater 260:707–714. https://doi.org/10.1016/j.jhazmat.2013.06.047
12. Rufino B, Boulch F, Coulet M-V et al (2007) Influence of particles size on thermal properties of aluminium powder. Acta Mater 55:2815–2827. https://doi.org/10.1016/j.actamat.2006.12.017
13. Hasani S, Panjepour M, Shamanian M (2014) Non-isothermal kinetic analysis of oxidation of pure aluminum powder particles. Oxid Met 81:299–313. https://doi.org/10.1007/s11085-013-9413-z
14. Hasani S, Panjepour M, Shamanian M (2012) The oxidation mechanism of pure aluminum powder particles. Oxid Met 78:179–195. https://doi.org/10.1007/s11085-012-9299-1
15. Hasani S, Soleymani AP, Panjepour M, Ghaei A (2014) A tension analysis during oxidation of pure aluminum powder particles: non-isothermal condition. Oxid Met 82:209–224. https://doi.org/10.1007/s11085-014-9488-1
16. Trunov MA, Schoenitz M, Zhu X, Dreizin EL (2005) Effect of polymorphic phase transformations in Al_2O_3 film on oxidation kinetics of aluminum powders. Combust Flame 140:310–318. https://doi.org/10.1016/j.combustflame.2004.10.010

17. Li L, Zou H, Cai S (2016) Thermal behaviour of gas atomised Al–20Mg–2Zr alloy powder. Mater Sci Technol 32:863–870. https://doi.org/10.1179/1743284715Y.0000000096

18. Legrand B, Marion M, Chauveau C et al (2001) Ignition and combustion of levitated magnesium and aluminum particles in carbon dioxide. Combust Sci Technol 165:151–174. https://doi.org/10.1080/00102200108935830

19. Zou H, Li L, Cai S (2016) Effect of magnesium-rich phase on oxidation properties of atomized aluminum–magnesium powders. J Propuls Power 32:32–37. https://doi.org/10.2514/1.B35781

20. Karimpour M, Eatezadi SR, Hasani S, Ghaei A (2019) The oxidation mechanism of pure magnesium powder particles: a mathematical approach. Metall Mater Trans B 50:1597–1607. https://doi.org/10.1007/s11663-019-01588-y

21. Aly Y, Hoffman VK, Schoenitz M, Dreizin EL (2014) Reactive, mechanically alloyed Al·Mg powders with customized particle sizes and compositions. J Propuls Power 30:96–104. https://doi.org/10.2514/1.B35031

22. Lomba R, Bernard S, Gillard P et al (2016) Comparison of combustion characteristics of magnesium and aluminum powders. Combust Sci Technol 188:1857–1877. https://doi.org/10.1080/00102202.2016.1211871

23. Kim K (2015) Formation of endogenous MgO and $MgAl_2O_4$ particles and their possibility of acting as substrate for heterogeneous nucleation of aluminum grains. Surf Interface Anal 47:429–438. https://doi.org/10.1002/sia.5726

24. Nie H, Schoenitz M, Dreizin EL (2016) Oxidation of magnesium: implication for aging and ignition. J Phys Chem C 120:974–983. https://doi.org/10.1021/acs.jpcc.5b08848

25. Shoshin YL, Mudryy RS, Dreizin EL (2002) Preparation and characterization of energetic Al-Mg mechanical alloy powders. Combust Flame 128:259–269. https://doi.org/10.1016/S0010-2180(01)00351-0

26. Xu C, Zou H, Cai S (2015) Thermal reactivity of Al–Mg–Li alloy powders. J Mater Res 30:2238–2246. https://doi.org/10.1557/jmr.2015.179

27. Corcoran AL, Wang S, Aly Y, Dreizin EL (2015) Combustion of mechanically alloyed Al•Mg powders in products of a hydrocarbon flame. Combust Sci Technol 187:807–825. https://doi.org/10.1080/00102202.2014.973951

28. Schoenitz M, Dreizin EL (2003) Structure and properties of Al–Mg mechanical alloys. J Mater Res 18:1827–1836. https://doi.org/10.1557/JMR.2003.0255

29. Matli P, Shakoor R, Amer Mohamed A, Gupta M (2016) Microwave rapid sintering of Al-metal matrix composites: a review on the effect of reinforcements. Microstruct Mech Prop Metals (Basel) 6:143. https://doi.org/10.3390/met6070143

30. Batool SA, Wadood A, Rehman MAU (2019) Comparison of aluminum based alloys reinforced with intermetallic developed by powder metallurgy and arc melting routes. Soldag Inspeção. https://doi.org/10.1590/0104-9224/si24.19

31. Faisal H, Darminto T, Zainuri M (2016) Interfacial reactions and wetting in Al-Mg sintered by powder metallurgy process. AIP Conf Proc 1725:020017. https://doi.org/10.1063/1.4945471

32. Yuan X, Qu X, Yin H et al (2019) Effects of compaction velocity on the sinterability of Al-Fe-Cr-Ti PM alloy. Materials (Basel) 12:3005. https://doi.org/10.3390/ma12183005

33. Starink M (2003) The determination of activation energy from linear heating rate experiments: a comparison of the accuracy of isoconversion methods. Thermochim Acta 404:163–176. https://doi.org/10.1016/S0040-6031(03)00144-8

34. Starink MJ (2007) Activation energy determination for linear heating experiments: deviations due to neglecting the low temperature end of the temperature integral. J Mater Sci 42:483–489. https://doi.org/10.1007/s10853-006-1067-7

35. Friedman HL (2007) Kinetics of thermal degradation of char-forming plastics from thermogravimetry. Application to a phenolic plastic. J Polym Sci Part C Polym Symp 6:183–195. https://doi.org/10.1002/polc.5070060121

36. Budrugeac P, Segal E, Pérez-Maqueda LA, Criado JM (2004) The use of the IKP method for evaluating the kinetic parameters and the conversion function of the thermal dehydrochlorination of PVC from non-isothermal data. Polym Degrad Stab 84:311–320. https://doi.org/10.1016/j.polymdegradstab.2004.01.017

37. Jaafari Z, Seifoddini A, Hasani S, Rezaei-Shahreza P (2018) Kinetic analysis of crystallization process in $[(Fe_{0.9}Ni_{0.1})77Mo5P9C7.5B1.5]100-xCux$ (x = 0.1 at.%) BMG. J Therm Anal Calorim 134:1565–1574. https://doi.org/10.1007/s10973-018-7372-y

38. Vyazovkin S, Burnham AK, Criado JM et al (2011) ICTAC kinetics committee recommendations for performing kinetic computations on thermal analysis data. Thermochim Acta 520:1–19. https://doi.org/10.1016/j.tca.2011.03.034

39. Khawam A, Flanagan DR (2006) Basics and applications of solid-state kinetics: a pharmaceutical perspective. J Pharm Sci 95:472–498. https://doi.org/10.1002/jps.20559

40. Hasani S, Shamanian M, Shafyei A et al (2014) Non-isothermal kinetic analysis on the phase transformations of Fe–Co–V alloy. Thermochim Acta 596:89–97. https://doi.org/10.1016/j.tca.2014.09.020

41. Rezaei-Shahreza P, Seifoddini A, Hasani S (2017) Non-isothermal kinetic analysis of nano-crystallization process in (Fe41Co7Cr15Mo14Y2C15)94B6 amorphous alloy. Thermochim Acta 652:119–125. https://doi.org/10.1016/j.tca.2017.03.017

42. Marinović-Cincović M, Janković B, Jovanović V et al (2013) The kinetic and thermodynamic analyses of non-isothermal degradation process of acrylonitrile–butadiene and ethylene–propylene–diene rubbers. Compos Part B Eng 45:321–332. https://doi.org/10.1016/j.compositesb.2012.08.006

43. Burnham AK, Dinh LN (2007) A comparison of isoconversional and model-fitting approaches to kinetic parameter estimation and application predictions. J Therm Anal Calorim 89:479–490. https://doi.org/10.1007/s10973-006-8486-1

44. Vyazovkin S, Wight CA (1999) Model-free and model-fitting approaches to kinetic analysis of isothermal and nonisothermal data. Thermochim Acta 340–341:53–68. https://doi.org/10.1016/S0040-6031(99)00253-1

45. Uzun N, Çolak AT, Emen FM, Çılgı GK (2016) The thermal and detailed kinetic analysis of dipicolinate complexes. J Therm Anal Calorim 124:1735–1744. https://doi.org/10.1007/s10973-016-5251-y

46. Ledeti A, Olariu T, Caunii A et al (2018) Evaluation of thermal stability and kinetic of degradation for levodopa in non-isothermal conditions. J Therm Anal Calorim 131:1881–1888. https://doi.org/10.1007/s10973-017-6671-z

47. Campostrini R, Abdellatief M, Leoni M, Scardi P (2014) Activation energy in the thermal decomposition of MgH$_2$ powders by coupled TG–MS measurements. J Therm Anal Calorim 116:225–240. https://doi.org/10.1007/s10973-013-3539-8

48. Singh A, Sharma TC, Kishore P (2017) Thermal degradation kinetics and reaction models of 1,3,5-triamino-2,4,6-trinitrobenzene-based plastic-bonded explosives containing fluoropolymer matrices. J Therm Anal Calorim 129:1403–1414. https://doi.org/10.1007/s10973-017-6335-z

49. Coats AW, Redfern JP (1964) Kinetic parameters from thermogravimetric data. Nature 201:68–69. https://doi.org/10.1038/201068a0

50. Gorbachev VM (1975) A solution of the exponential integral in the non-isothermal kinetics for linear heating. J Therm Anal 8:349–350. https://doi.org/10.1007/BF01904012

51. Gallet J-J, Silly MG, El KM et al (2017) Chemical and kinetic insights into the thermal decomposition of an oxide layer on Si(111) from millisecond photoelectron spectroscopy. Sci Rep 7:14257. https://doi.org/10.1038/s41598-017-14532-4

52. Al Soubaihi R, Saoud K, Dutta J (2018) Critical review of low-temperature CO oxidation and hysteresis phenomenon on heterogeneous catalysts. Catalysts 8:660. https://doi.org/10.3390/catal8120660

53. Kasap S, Málek J, Svoboda R (2017) Thermal properties and thermal analysis: fundamentals, experimental techniques and applications. Springer Handbook of Electronic and Photonic Materials. Springer International Publishing, Cham, pp 1–1

54. Hasani S, Panjepour M, Shamanian M (2012) Effect of atmosphere and heating rate on mechanism of MoSi$_2$ formation during self-propagating high-temperature synthesis. J Therm Anal Calorim. https://doi.org/10.1007/s10973-011-1747-7

55. Sanchez ME, Otero M, Gómez X, Morán A (2009) Thermogravimetric kinetic analysis of the combustion of biowastes. Renew Energy 34:1622–1627. https://doi.org/10.1016/j.renene.2008.11.011

56. Vyazovkin S, Chrissafis K, Di Lorenzo ML et al (2014) ICTAC kinetics committee recommendations for collecting experimental thermal analysis data for kinetic computations. Thermochim Acta 590:1–23. https://doi.org/10.1016/j.tca.2014.05.036

57. Hasani S, Panjepour M, Shamanian M (2010) A study of the effect of aluminum on MoSi$_2$ formation by self-propagation high-temperature synthesis. J Alloys Compd. https://doi.org/10.1016/j.jallcom.2010.04.159

58. Xu C, Gao W (2000) Pilling-Bedworth ratio for oxidation of alloys. Mater Res Innov 3:231–235. https://doi.org/10.1007/s100190050008

59. Tan Q, Atrens A, Mo N, Zhang M-X (2016) Oxidation of magnesium alloys at elevated temperatures in air: a review. Corros Sci 112:734–759. https://doi.org/10.1016/j.corsci.2016.06.018
60. Khawam A, Flanagan DR (2006) Solid-state kinetic models: basics and mathematical fundamentals. J Phys Chem B 110:17315–17328. https://doi.org/10.1021/jp062746a
61. Erceg M, Kovačić T, Perinović S (2008) Kinetic analysis of the non-isothermal degradation of poly(3-hydroxybutyrate) nanocomposites. Thermochim Acta 476:44–50. https://doi.org/10.1016/j.tca.2008.07.009
62. Vrandečić NS, Erceg M, Jakić M, Klarić I (2010) Kinetic analysis of thermal degradation of poly(ethylene glycol) and poly(ethylene oxide)s of different molecular weight. Thermochim Acta 498:71–80. https://doi.org/10.1016/j.tca.2009.10.005

Publisher's Note Springer Nature remains neutral with regard to jurisdictional claims in published maps and institutional affiliations.